SCIENCE CHINA
Chemistry

•ARTICLES•

June 2023 Vol.66 No.6: 1860–1868
https://doi.org/10.1007/s11426-023-1583-8

Tunable catalytic activity of $FeWO_4$ nanomaterials for sensitive assays of pyrophosphate ion and alkaline phosphatase activity

Xianqing Tang[1,2], Jinghuang Chen[1,2], Mengqian Zhang[1,3], Jian Sun[1*] & Xiurong Yang[1,2*]

[1]*State Key Laboratory of Electroanalytical Chemistry, Changchun Institute of Applied Chemistry, Chinese Academy of Sciences, Changchun 130022, China;*
[2]*School of Applied Chemistry and Engineering, University of Science and Technology of China, Hefei 230026, China;*
[3]*Department of Chemistry, University of Science and Technology of China, Hefei 230026, China*

Received February 21, 2023; accepted March 27, 2023; published online May 8, 2023

Alkaline phosphatase (ALP) activity and pyrophosphate ion (PPi) levels are remarkable for the human body functions such as signal transduction pathways and metabolism. Current quantitative methods mainly focus on developing complicated organic substrates or employing unstable metal ions as signal-regulated medium. Herein, we have developed a facile hydrothermal method for preparing $FeWO_4$ nanomaterials with intrinsic peroxidase-like activity and further confirmed that such a catalytic activity could be significantly enhanced by adjusting the size and oxygen vacancy content. More encouragingly, PPi can easily inhibit the catalytic activity of $FeWO_4$, whereas orthophosphate ions (Pi) cannot. Therefore, we constructed an $FeWO_4$-based colorimetric assay for sensing PPi by means of the classical 3,3′,5,5′-tetramethylbenzidine-peroxidase chromogenic reaction. A facile and reliable ALP activity assay was also designed and developed because of the logical regulation of the peroxidase-like activity of $FeWO_4$ through the ALP-catalyzed hydrolysis of PPi into Pi. Based on the clear mechanism and mimetic-enzyme $FeWO_4$-catalyzed amplification, the sensing system exhibited excellent performance and was able to evaluate ALP activity in real serum samples and screen for potential ALP inhibitors. The proposed mimetic enzyme-involved colorimetric assay provides an alternative pathway, and $FeWO_4$ nanomaterials with excellent performance have great potential for further biosensing and biomedical applications.

$FeWO_4$ nanomaterials, mimetic enzyme, oxygen vacancy, colorimetry, pyrophosphate ion, alkaline phosphatase

Citation: Tang X, Chen J, Zhang M, Sun J, Yang X. Tunable catalytic activity of $FeWO_4$ nanomaterials for sensitive assays of pyrophosphate ion and alkaline phosphatase activity. *Sci China Chem*, 2023, 66: 1860–1868, https://doi.org/10.1007/s11426-023-1583-8

1 Introduction

As a zinc-containing dimer enzyme, alkaline phosphatase (ALP) is widely distributed in various tissues (liver, kidney, bone, placenta, and intestine) [1]. It plays a vital role in the hydrolysis process of various phosphate esters in organisms, and can achieve a high catalytic rate under an alkaline environment [2]. Thus, ALP plays a key role in the cell cycle, growth, apoptosis, and signal transduction pathways, and is involved in the transduction and regulation of intracellular processes [3]. Meanwhile, abnormal ALP levels have been linked to various diseases (breast cancer, diabetes, ovarian, and bone diseases), making it a useful biomarker in clinical diagnosis [4,5]. Therefore, it is important to develop a sensitive method for evaluating ALP activity [6,7].

ALP activity assays mainly involve the differentiation between a phosphoryl substrate and the corresponding enzymatic product, and several substrates have been developed in the past, such as pyrophosphate (PPi) [8], ascorbic acid phosphate [9], *p*-nitrophenyl phosphate [10], and 5-bromo-4-chloro-3-indolyl phosphate [11]. As the simplest substrate molecule among these substrates, PPi is an important bio-

---

*Corresponding authors (email: xryang@ciac.ac.cn; jiansun@ciac.ac.cn)

logical inorganic phosphate and participates in many important biological systems [12,13]. For instance, PPi is involved in several biological processes, such as gene replication [14], gene transcription [15], signal transduction [16], and regulation of various enzymatic reactions [17]. Meanwhile, abnormal PPi levels are closely linked to certain severe diseases [18,19]. Therefore, efficient PPi identification and detection can not only realize the evaluation of ALP levels, but also have the potential to be used for environmental protection and human health monitoring.

In recent years, nanomaterials with enzyme mimetics have garnered considerable attention for their excellent performance in catalyzing certain substrates and producing readable signals in bioanalytical applications [20]. Among them, the catalytic activity of transition metal-based materials is often affected by phosphate groups because of their strong binding ability [21]. Inspired by this phenomenon, transition metal-based materials, such as transition metal oxides (MnO_2 microspheres) [22], hydroxides (CoOOH) [23], and framework materials (Cu-MOF) [24], have been developed to determine and evaluate PPi levels and ALP activity. Despite their potential, there are still challenges to be overcome owing to the inherent defects of such materials and their ambiguous catalytic mechanism.

Thus, the development of enzyme-mimetic nanomaterials with excellent stability and responsiveness is important for the construction of analytical determination of PPi and ALP. As one of such materials, the recently emerged novel nanomaterial iron tungstate ($FeWO_4$), has exhibited an excellent catalytic effect in photocatalysis and electrocatalysis and possesses a significant potential in enzyme-mimetic catalysis [25,26]. Herein, $FeWO_4$ nanomaterials with excellent peroxidase-like properties were prepared through a facile hydrothermal method in one step. By adjusting their size and oxygen vacancy content to regulate their catalytic activity, it was verified that a variety of reactive oxygen species were generated during the catalytic reaction with Fe atoms as the active center. In this regard, the size and defect effects of the mimetic enzyme enhance its peroxidase-like activity by favoring the exposure of Fe atoms and vacancies. More interestingly, $FeWO_4$ nanomaterials can selectively bind with PPi, inhibiting its peroxidase-like activity, while the inhibition efficiency of Pi is low. Accordingly, ALP can restore the catalytic activity of the $FeWO_4$ nanomaterials by cleaving the PPi substrate into Pi. Based on this, we successfully constructed an evaluation system for ALP and PPi using the as-prepared $FeWO_4$ nanomaterials with the best catalytic performance. The experimental results demonstrate that the proposed sensing system has a lower detection limit and higher sensitivity than most previously reported biosensors, indicating that this system has significant potential for future biosensing applications.

2 Experimental

2.1 Chemical and materials

Ethylene glycol (EG), H_2O_2 30%, iron(II) sulfate heptahydrate ($FeSO_4 \cdot 7H_2O$), nickel chloride hexahydrate ($NiCl_2 \cdot 6H_2O$), iron(III) sulfate ($Fe_2(SO_4)_3$), anhydrous calcium chloride ($CaCl_2$), magnesium chloride hexahydrate ($MgCl_2 \cdot 6H_2O$), ammonium sulfate ($(NH_4)_2SO_4$), potassium thiocyanate (KSCN), potassium chloride (KCl), and anhydrous potassium carbonate (K_2CO_3) were purchased from Xilong Scientific Co, Ltd. (China). Sodium tungstate dihydrate ($Na_2WO_4 \cdot 2H_2O$), sodium pyrophosphate (PPi), potassium phosphate tribasic (K_3PO_4), acetic acid (HAc), cadmium acetate (CdAc), zinc sulfate ($ZnSO_4 \cdot 7H_2O$), and sodium chloride (NaCl) were purchased from Aladdin Co, Ltd. (China). Chromium(III) chloride hexahydrate ($CrCl_3 \cdot 6H_2O$) was purchased from Sinopharm Chemical Reagent Co, Ltd. (China). Copper chloride ($CuCl_2 \cdot 2H_2O$), sodium nitrate ($NaNO_3$), aluminum nitrate nonahydrate ($Al(NO_3)_3 \cdot 9H_2O$), ammonium chloride (NH_4Cl), and sodium bromide (NaBr) were purchased from Beijing Chemical Corp. (China). Cobalt chloride ($CoCl_2$), diethanolamine (DEA), tyrosinase (TYR, from mushroom), cholesterol oxidase (Cholx, from recombinant expressed *E. coli*), glucose oxidase (Gox, from Aspergillus niger), acetylcholinesterase (AChE, from Electrophorus electricus), lysozyme (LYZ, from chicken eggs), choline oxidase (ChOx, from *Alcaligenes* sp.), and trypsin (TRY, from bovine pancreas) were purchased from Sigma-Aldrich (USA). Sodium orthovanadate dodecahydrate ($Na_3VO_4 \cdot 12H_2O$) and 3,3′,5,5′-tetramethylbenzidine dihydrochloride (TMB) were purchased from Sangon Biotech Co, Ltd. (China). Normal adult serum samples were donated by the Secondary Hospital of Jilin University.

2.2 Instrumentation

Scanning electron microscopy (SEM) images were obtained using an XL-30 field-emission scanning electron microscope. UV-VIs absorption spectra were recorded on a CARY 50UV-Vis-NIR Varian spectrophotometer. Transmission electron microscopy (TEM) images were obtained using a TECNAI F20 microscope (FEI, USA) at an accelerating voltage of 200 kV. X-ray powder diffusion (XRD) patterns of all the samples were obtained using a D8 ADVANCE (Bruker, Germany). Fourier-transform infrared spectroscopy (FTIR) images were obtained using a Vertex 70 spectrometer (Bruker, Germany). X-ray photoelectron spectroscopy (XPS) was performed using a Thermo ESCALAB 250XI spectrometer (UK). Electron paramagnetic resonance (EPR) spectroscopy was performed using a Bruker EMXPLUS instrument (Germany). The Brunauer-Emmett-Teller (BET) surface area was determined from N_2 adsorption-desorption isotherms obtained at 298 K using an Autosorb iQ Station 1 instrument (USA).

2.3 Preparation and purification of $FeWO_4$

$FeWO_4$ was prepared using a one-step hydrothermal method as follows: 0.83 mmol $FeSO_4 \cdot 7H_2O$ was dissolved in certain H_2O, and EG was subsequently added to the solution. Finally, the preconfigured 0.83 mmol $Na_2WO_4 \cdot 2H_2O$ solution was added to the obtained solution. The total volume of the solution was approximately 33 mL. After stirring for 30 min, the solution became uniform and was transferred into an autoclave and heated at 160 °C for 12 h. The resulting precipitates were washed thrice with deionized water, ethanol, and a mixture of deionized water and ethanol through centrifugation, respectively. Finally, the resulting product was placed in a vacuum-drying oven at 50 °C overnight and stored for future use.

2.4 Peroxidase-mimetic activity and kinetic parameters of the obtained $FeWO_4$ nanocrystal

The peroxidase-like catalytic behavior of the $FeWO_4$ nanomaterials was investigated through the oxidation of TMB in the presence of H_2O_2 and four groups were studied: H_2O_2 + TMB, FWO + H_2O_2, FWO + TMB, and FWO + H_2O_2 + TMB. The mimetic-enzyme activity assays were performed as follows: 100 μL of $FeWO_4$ (1 mg/mL), 40 μL of TMB (7.5 mM), and 2,660 μL of sodium acetate buffer (50 mM, pH 4.0) were added. Subsequently, 200 μL of H_2O_2 (7.5 mM) was mixed thoroughly. After incubation at room temperature for 15 min, the mixture was transferred to a UV-vis spectrophotometer, and the absorbance at 652 nm was recorded. The tolerance of $FeWO_4$ peroxidase mimetic activity to temperature (10–80 °C) and pH (2.5–9.0) was also investigated, and the maximum activity values measured in each group were expressed as 100% after normalization.

The absorbance variation of the FWO/H_2O_2/TMB system at 652 nm was recorded at regular intervals in scanning kinetic mode using a UV-vis spectrophotometer. The kinetic data of the FWO peroxidase mimetic were determined using the Lineweaver-Burk equation as follows:

$$v_0 = \frac{V_{\max} \times [S]}{K_m + [S]}$$

where v_0 represents the initial velocity of the reaction, $V_{\max}$ is the maximum velocity of the reaction, $[S]$ is the substrate (TMB or H_2O_2) concentration in the reaction solution, and K_m is the Michaelis-Menten constant.

2.5 Procedure for the assay of PPi

Briefly, 100 μL of $FeWO_4$ (1 mg/mL), different concentrations of PPi, and 40 μL of TMB (7.5 mM) were added to a 5 mL centrifugation tube, and the solution was supplemented with sodium acetate buffer (50 mM, pH 4.0) to 2,800 μL. After mixing, 200 μL H_2O_2 (7.5 mM) was added. After incubation at room temperature for 15 min, the solution was transferred to a UV-vis spectrophotometer to record the spectra.

2.6 Procedure for the assay of ALP

Typically, 100 μL of PPi (60 μM), 50 μL of different concentrations of ALP, and 350 μL of DEA buffer (4 mM, pH 9.8) were mixed in a 5 mL centrifugation tube and incubated at 37 °C for 60 min. Subsequently, 2,260 μL of sodium acetate buffer (50 mM, pH 4.0), 100 μL of FWO (1 mg/mL), 40 μL of TMB (7.5 mM), and 200 μL of H_2O_2 (7.5 mM) were added to the obtained solution and incubated at 25 °C for 15 min. Finally, the absorption spectra of the solution were collected using the UV-vis spectrophotometer.

3 Results and discussion

3.1 Preparation and characterization of $FeWO_4$

As illustrated in Scheme 1, a series of $FeWO_4$ nanomaterials were prepared through a one-step hydrothermal method using $FeSO_4 \cdot 7H_2O$ and $Na_2WO_4 \cdot 2H_2O$ as precursors in the presence of different volume proportions of EG and H_2O. Depending on the added concentrations of EG (0, 10%, 30%, 50%, 70%, and 90%,) to the total reaction solutions, the as-obtained products are named as FWO-0, FWO-0.1, FWO-0.3, FWO-0.5, FWO-0.7 and FWO-0.9, respectively.

TEM characterization indicated that the size of the nanoparticles decreased from FWO-0 to FWO-0.9 (Figure 1a–f and Figure S1, Supporting Information online). This could be attributed to the fact that the addition of EG limited the growth of FWO nanoparticle crystals, resulting in a reduction in the size of the formed nanoparticles [27]. When there was no EG or a very low EG concentration, the as-prepared FWO-0 and FWO-0.1 were both composed of nanosheets and nanoparticles, while when the added EG content reached 30% and beyond, the obtained products (FWO-0.3, FWO-0.5, FWO-0.7, and FWO-0.9) contained only nanoparticles. Taking FWO-0.7 as an example, the scanning transmission electron microscopy (STEM) and element mapping images exhibited a uniform distribution of Fe, W, and O in the resultant FWO-0.7 nanoparticles (Figure 1h–k). At the same time, high-resolution TEM (HRTEM) images showed that the as-prepared FWO-0.7 nanoparticles had interplanar spacings of 0.478 and 0.298 nm, which corresponded to the (100) and (111) crystal planes of $FeWO_4$, respectively (Figure 1g) [28]. Furthermore, the BET results indicated that the specific surface areas of the as-prepared FWO-0,

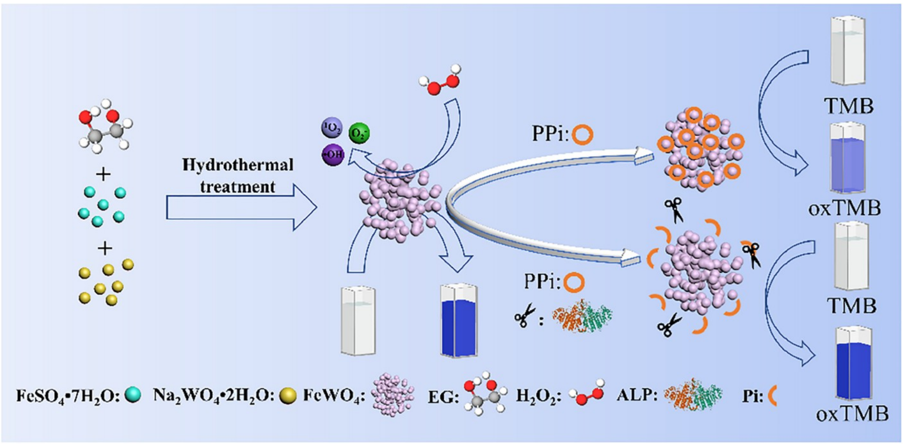

Scheme 1 Preparation of $FeWO_4$ and establishment of a sensing platform for PPi concentration and ALP activity assays (color online).

FWO-0.1, FWO-0.3, FWO-0.5, FWO-0.7, and FWO-0.9 nanomaterials were 40.25, 32.53, 15.01, 23.92, 78.46, and 98.74 m^2/g, respectively (Figure S2). It could be observed that the specific surface area of the nanomaterials gradually increased from FWO-0.3 to FWO-0.9, which may be attributed to the gradual increase in specific surface area as the size of the prepared nanomaterials decreased. By comparison, nanomaterials with large specific surface areas provide more binding sites for the adsorption and desorption of reactions, which facilitates further catalytic activity enhancement [29]. Besides, the specific surface area of FWO-0.3 was smaller than that of FWO-0 and FWO-0.1, which may be due to the mixing of nanosheets and nanoparticles in FWO-0 and FWO-0.1, and the fact that the nanosheets increased the specific surface area. This result is consistent with that of previous TEM characterizations.

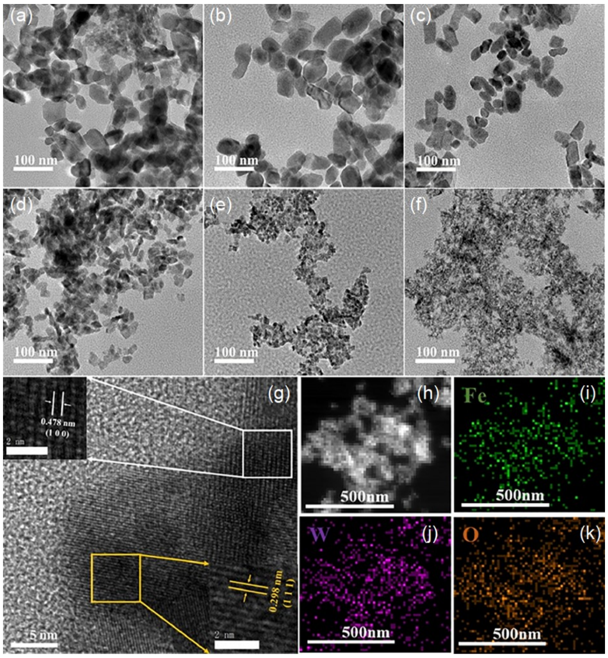

Figure 1 (a–f) TEM images of FWO-0–FWO-0.9. (g) HRTEM image of FWO-0.7. (h) HAADF-STEM image and (i) Fe; (j) W, and (k) O element mapping images of FWO-0.7 (color online).

The FTIR spectra showed that the main peaks of the as-prepared FWO nanomaterials were similar (Figure S3). The peaks at approximately 3,423 and 1,624 cm^{-1} can be attributed to –OH stretching and the bending vibration of water in the FWO solution, respectively. The 864 and 625 cm^{-1} characteristic peaks are attributed to the W–O and Fe–O stretching vibrations, respectively [30,31]. Besides, the Raman spectrum (Figure S4) indicates that the peak at 866 cm^{-1} is attributed to the endpoint v_1 symmetric A_g mode of WO_2, whereas the broad peak at 675 cm^{-1} originates from the v_3 antisymmetric bridge mode associated with the tungstate chain [32,33]. The peak at 340 cm^{-1} corresponds to the v_2 bending model, and the peaks at 278 and 210 cm^{-1} correspond to the v_4 bending model of the tungstate anion [34]. The peaks at 125 and 81 cm^{-1} are attributed to lattice vibrations [35]. It was demonstrated that the as-prepared products were consistent with those of previously reported $FeWO_4$ nanomaterials.

Furthermore, the XRD spectra of FWO-0–FWO-0.9 showed that the peaks of all the FWO nanomaterials are in accordance with the standard XRD diagram of $FeWO_4$ (JCPDS.No.85-1354), indicating the successful preparation of $FeWO_4$ (Figure 2a). In addition, it was observed that the width of the FWO peaks gradually broadened from FWO-0 to FWO-0.9, indicating the reduction of the crystallinity. This may be related to the appearance of oxygen vacancies and the reduction in the nanomaterial size [36]. To further confirm the existence of oxygen vacancies, we selected FWO-0, FWO-0.3, and FWO-0.7, and used EPR to further characterize the vacancies. Figure 2b shows that the prepared $FeWO_4$ nanomaterials exhibit characteristic oxygen vacancy signals with a *g*-factor of approximately 2.003. The progressively increasing signal intensity from FWO-0 to FWO-0.7 confirms the increase in the oxygen vacancy concentration.

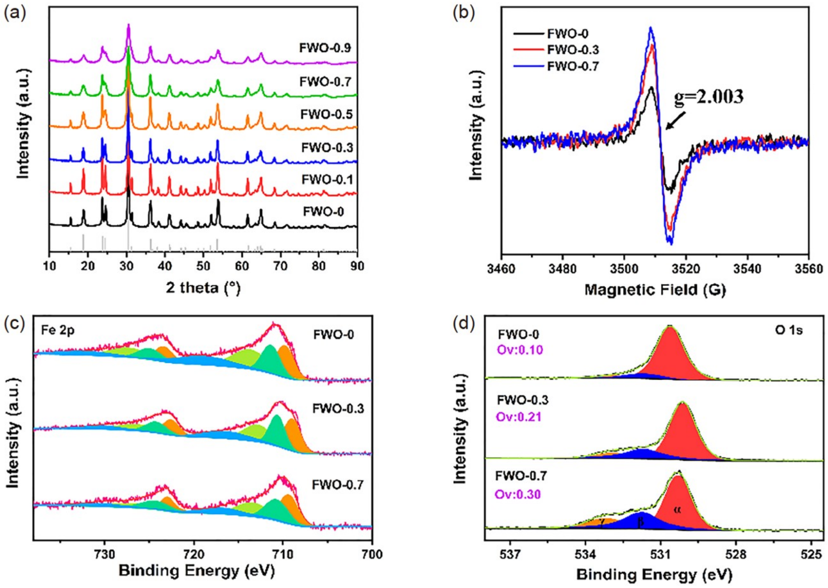

Figure 2 (a) XRD patterns of the series of $FeWO_4$ nanomaterials and (b) room-temperature EPR spectra of FWO-0, FWO-0.3, and FWO-0.7. XPS spectra of (C) Fe 2p and (d) O 1s for FWO-0, FWO-0.3, and FWO-0.7 (color online).

The XPS survey spectrum illustrated in Figure S5a shows that the as-prepared sample contains three elements: Fe, W, and O, and their signals are approximately 709.67, 36.21, and 530.98 eV, respectively [37]. In the Fe 2p XPS spectrum, the peaks are approximately 709.37 and 724.33 eV (Figure 2c), which correspond to Fe^{2+} ($2p_{3/2}$) and Fe^{2+} ($2p_{1/2}$), respectively [38]. This result confirmed that the prepared sample contained Fe^{2+}, indicating the successful preparation of $FeWO_4$. Figure S5b shows the XPS spectra of W 4f; the peaks at 35.22 and 37.37 eV correspond to W^{6+} ($4f_{7/2}$) and W^{6+} ($4f_{5/2}$), respectively [39]. The XPS spectrum of O 1s shows that the α peak at 530.29 eV corresponds to lattice oxygen, which is formed by the combination of W and O bonds. The β peak at 531.71 eV corresponds to the defective oxygen and the γ peak of 533.16 eV corresponds to the chemisorbed oxygen on the sample surface (Figure 2d) [40]. The increase in the relative area of oxygen vacancies (O_v) from FWO-0 to FWO-0.7 shows that the oxygen vacancy content of the prepared $FeWO_4$ increases gradually, which is consistent with the EPR results. These results not only confirmed the successful preparation of $FeWO_4$ but also demonstrated that with the increase in EG concentration added in the initial reaction, the size of the $FeWO_4$ nanomaterials gradually decreased but the content of oxygen vacancies gradually increased.

3.2 Peroxidase-mimetic activity and catalytic mechanism of FWO

In this study, we used the TMB/H_2O_2 system to evaluate the peroxidase-mimetic activity of $FeWO_4$. As shown in Figure 3a, the FWO-0.7/TMB/H_2O_2, FWO-0.7/TMB, FWO-0.7/H_2O_2, and TMB/H_2O_2 systems were incubated, and the solutions were recorded in the UV-vis absorption spectra. Obviously, only FWO-0.7/TMB/H_2O_2 was observed to have a clear absorption peak at 652 nm, whereas no obvious absorption peak was observed in the other systems. The results demonstrated that FWO-0.7 facilitated the oxidation of colorless TMB to colored oxTMB in the presence of H_2O_2. However, FWO-0.7 could not oxidize TMB on its own, revealing its peroxidase-like properties.

The peroxidase-like activity of the $FeWO_4$ nanomaterials was evaluated and the order of activity was as FWO-0.7≈FWO-0.9>FWO-0.5>FWO-0.3>FWO-0.1>FWO-0 (Figure 3b). It was demonstrated that the reduced size and increased oxygen vacancies may be beneficial for increasing the catalytic activity of $FeWO_4$. Among them, because FWO-0.9 may be too small in size and thus prone to stacking and is not easily dispersed, FWO-0.7 was used in the subsequent sensing experiments. In addition, bulk $FeWO_4$ was prepared by employing Fe^{3+} as a precursor to explore the effects of Fe^{3+} and Fe^{2+} on the catalytic activity (Figure S6). The results demonstrate that the small nanoparticles of FW0-0.7 prepared from Fe^{2+} exhibit better catalytic activity than the Fe^{3+}-participated bulk $FeWO_4$. This difference may be due to the gradual reduction of Fe^{3+} to Fe^{2+} by EG during the reaction, which constantly generated Fe^{2+}, forming new $FeWO_4$ gradually wrapped on the surface of the old $FeWO_4$ crystal, and causing the $FeWO_4$ crystal to grow larger and larger. Instead, Fe^{2+} is directly combined with WO_4^{2-} to produce a smaller FWO-0.7 [41]. Therefore, the smaller FWO-0.7, synthesized directly using Fe^{2+}, has a larger specific surface area and higher catalytic activity than Fe^{3+}-participated bulk $FeWO_4$.

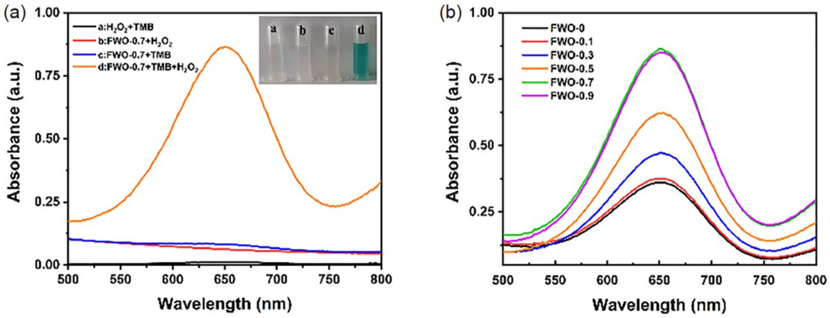

Figure 3 (a) UV-vis absorption spectra of different reaction systems. Inset shows the photos of the corresponding systems. (b) UV-vis absorption spectra of FWO prepared using different EG concentrations reacted with TMB-H_2O_2 for 15 min (color online).

Similar to natural horseradish peroxidase (HRP), the reaction time, pH, and temperature of the as-prepared $FeWO_4$ mimetic enzyme are also important factors that affect enzyme activity. Therefore, these conditions were optimized, and the optimal reaction time, pH, and temperature conditions were 25 min, 4.0, and 35 °C, respectively (Figure S7). In addition, we examined the reproducibility of the catalytic activity of FWO-0.7. Figure S8a shows that several different batches of FWO-0.7 were prepared, and there was no significant difference in the activity of these products under the same catalytic conditions, indicating that the prepared FWO-0.7 exhibited excellent reproducibility of the catalytic activity. Besides, the stability of FWO-0.7 (Figure S8b) showed that under the same catalytic conditions, the prepared FWO-0.7 did not exhibit a significant decrease in reactivity within 30 days. Figure S8c, d show that the prepared FWO-0.7 nanomaterials still have good reusability and stability despite multiple reuse and extreme conditions treatment, respectively.

Kinetic analyses of FWO-0, FWO-0.3, and FWO-0.7 were conducted to quantify the peroxidase-mimetic activity of FWO. As shown in Figure S9, using H_2O_2 and TMB as substrates, typical Michaelis-Menten curves were obtained by fixing the concentration of one substrate and varying the concentration of the other. Regarding the kinetics of either TMB or H_2O_2 as substrates, V_{max} gradually increased from FWO-0 to FWO-0.7. Meanwhile, the k_{m} values of FWO-0.7 using TMB and H_2O_2 as substrates were 0.080 and 0.878 mM, respectively, both of which are lower than those of HRP and most mimetic-enzymes reported so far, indicating that FWO-0.7 has a high affinity to substrates, facilitating catalyst-substrate binding and substrate activation (Table S1, Supporting Information online) [42].

To further reveal the catalytic mechanism of FWO, selective scavengers such as *p*-benzoquinone (PBQ), tryptophan (Trp), and isopropanol (IPA) were used to eliminate superoxide anions ($O_2^{\bullet-}$), singlet oxygen ($^1O_2$), and hydroxyl radicals (·OH), respectively, to verify the type of reactive oxygen species (ROS) in the catalytic reaction (Figure 4a) [43,44]. It was observed that IPA slightly decreased the reaction activity, whereas Trp and PBQ significantly decreased the relative reaction activity after adding these three substances, respectively, indicating that the ROS produced in the reaction are mainly $O_2^{\bullet-}$, $^1O_2$, and a small amount of ·OH. Furthermore, terephthalic acid (TA) was used as a fluorescent indicator to detect ·OH generation in the reaction [45]. As shown in Figure 4b, a significant fluorescence enhancement was observed at 435 nm after the addition of FWO-0.7, indicating that ·OH was indeed generated in this reaction, which is consistent with previous experimental results of the trapping agent. Similarly, the EPR spectra showed that when FWO-0.7 was mixed with H_2O_2, a total of three free radical peaks appeared, which was consistent with previous experimental results (Figure 4c). KSCN is one of the classical chelating agents used for Fe atom poisoning, which is used to investigate the catalytic activity of Fe atom in reactions. As illustrated in Figure 4d, the absorbance of the reaction system was significantly reduced after KSCN was added to the FWO-0.7/H_2O_2/TMB system, perhaps suggesting that the Fe atom of FWO-0.7 may be an important active site in the reaction system [46]. In summary, it is speculated that the reaction mechanism may be that H_2O_2 first combines with Fe atoms to produce $O_2^{\bullet-}$, $^1O_2$, and ·OH under the catalysis of the Fe atom, some $^1O_2$ may be further transformed into $O_2^{\bullet-}$, and the $O_2^{\bullet-}$, $^1O_2$, and ·OH radicals oxidize TMB into blue oxidized TMB (oxTMB) [47].

3.3 Sensitive measurement of PPi content

FWO-0.7 was selected for further bioanalytical applications owing to its excellent catalytic properties and dispersion. And it was observed that the oxidation of colorless TMB to blue oxTMB was inhibited after adding PPi to the FWO-0.7/TMB/H_2O_2 system, perhaps suggesting that PPi can bind to the catalytic central Fe site, thus decreasing the catalytic activity [48].

As shown in Figure 5a, b, PPi with different concentrations (0–10,000 nM) was added to the FWO-0.7/TMB/H_2O_2 system respectively, and the absorbance at 652 nm gradually weakened with the increase in PPi concentration. Mean-

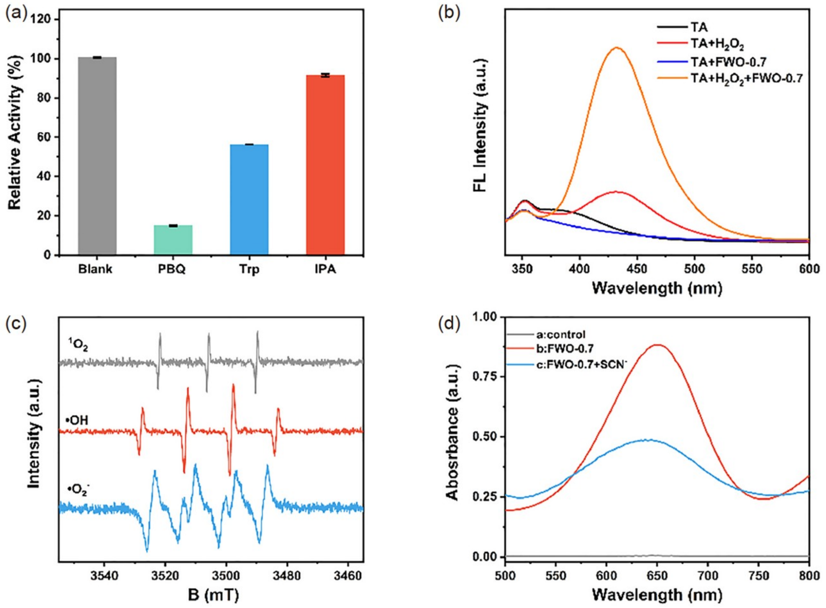

Figure 4 (a) Effect of different free radical scavengers on the catalytic reaction. (b) Fluorescent spectra of TA with different reaction systems. (c) EPR spectra of FWO-0.7 + H_2O_2. (d) UV-vis absorption spectra and the corresponding color of TMB-H_2O_2 (line a), TMB-H_2O_2 with FWO-0.7 (line b), and FWO-0.7 + SCN^- (line c) (color online).

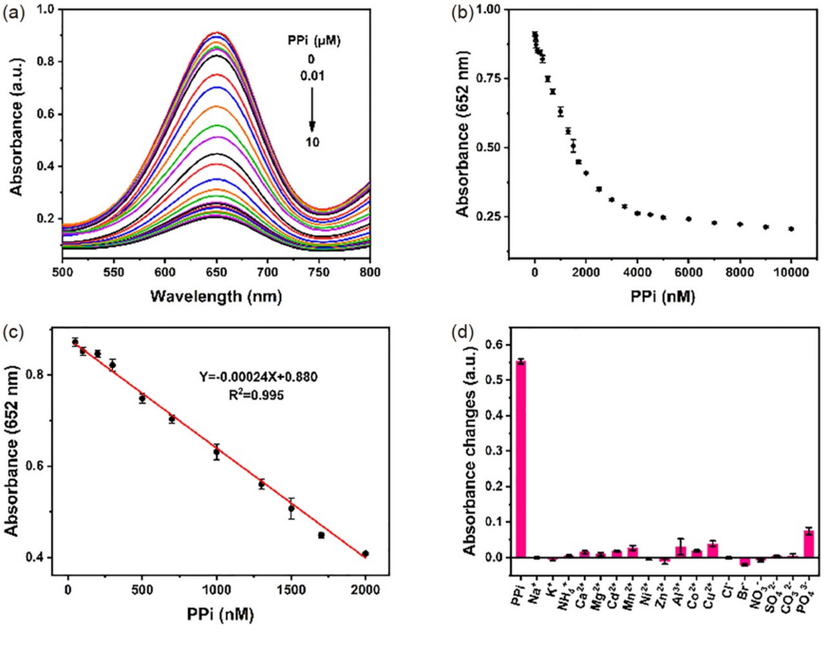

Figure 5 (a) UV-vis absorption spectra and (b) absorbance of the FWO-0.7 colorimetric system with different concentrations of PPi at 652 nm. (c) The fitting linear curve of absorbance and PPi concentration at 652 nm. (d) The changes of the absorbance at 652 nm refering to the interference to the FWO-0.7 colorimetric system in the presence of PPi or other substances (absorbance change refers to the difference of absorbance values in the absence and presence of interference). The concentrations of interfering substances are 100 μM of Na^+, K^+, NH_4^+, Ca^{2+}, Mg^{2+}, Cd^+, Mn^{2+}, Ni^{2+}, Zn^{2+}, Al^{3+}, Co^{2+}, Cl^-, Br^-, NO_3^-, SO_4^{2-}, and CO_3^{2-}; 50 μM of Cu^{2+}; 3 μM of PO_4^{3-}; and 2 μM of PPi (color online).

while, when the curve range was 50–2,000 nM, the concentration of PPi was linear with the absorbance at 652 nm, and the linear equation was obtained by fitting the curve: $y = -0.00024x + 0.880$ ($R^2 = 0.995$) (Figure 5c). The limit of detection (LOD) was determined as 30.2 nM ($3\sigma/S$). In comparison with most reported PPi sensing systems, the obtained results exhibited a lower detection limit and a more sensitive detection range, which has significant potential for future applications (Table S2). To further verify the anti-interference ability of the proposed sensing system, a series of ions were selected as interference substances, including Na^+, K^+, NH_4^+, Ca^{2+}, Mg^{2+}, Cd^+, Mn^{2+}, Ni^{2+}, Zn^{2+}, Al^{3+}, Co^{2+}, Cu^{2+}, Cl^-, Br^-, NO_3^-, SO_4^{2-}, CO_3^{2-}, and PO_4^{3-}. As illustrated in Figure 5d, the corresponding ions added to the system only slightly change the absorbance change at 652 nm, indicating that the sensor based on the FWO-0.7/H_2O_2/TMB system for PPi assays has excellent selectivity and anti-interference ability. Considering the excellent sensitivity and selectivity of the FWO-0.7/H_2O_2/TMB system, real samples (tap and lake water) were further applied to the PPi assay (Table S3). The recoveries ranged from 100.41% to 106.74%, and the relative standard deviations (RSD) were less than 3.28%, indicating that the proposed system can be used for practical applications.

3.4 Sensitive evaluation of ALP activity

In particular, it was observed that Pi induced a slight change in activity in the PPi selectivity test (Figure 5d). Likewise, ALP hydrolyzed PPi and degraded it into Pi fragments, restoring the catalytic activity of the inhibited FWO-0.7/H_2O_2/TMB system. This result indicates that it is possible to evaluate the activity of ALP through the re-oxidation of colorless TMB to blue oxTMB. As illustrated in Figure 6a, b, the absorbance at 652 nm of the inhibited FWO-0.7/TMB/H_2O_2 system increased with an increase in ALP activity, indicating that the inhibited color development system gradually recovered. Figure 6c shows that the absorbance centered at 652 nm has an excellent linear relationship with ALP activity in the range of 0.05–0.6 mU/mL. The linear equation resulting from the fitting can be expressed as $y = 0.604x + 0.372$ ($R^2 = 0.995$), and the LOD was evaluated as 0.0079 mU/mL ($3\sigma/S$), indicating that this method exceeds the detection limit and sensitivity of previously reported methods (Table S4). Subsequently, several enzymes such as AChE, ChOx, GOx, TRY, TYR, LYZ, and COD were added to test the effect on the color system with or without ALP, and the results are illustrated in Figure 6d. All added enzymes did not significantly affect the signal of the reaction system or interfered with the ALP activity, manifesting an excellent selectivity. Inspired by the excellent performance of the colorimetric system for ALP activity, the ALP activity in diluted serum was further evaluated. Table S5 lists excellent recoveries ranging from 98.46% to 105.11% with RSD less than 3.42%, indicating potential for future clinical diagnosis.

Screening inhibitors are of great significance in drug discovery and development. Here, we took Na_3VO_4, a classic inhibitor of ALP, as an example to develop the screening of inhibitors based on the determination of ALP. As illustrated in Figure 6e, f, as the concentration of Na_3VO_4 increases from 0.1 to 500 μM, we obtained a classical S-shaped curve of the change between the absorbance at 652 nm and the logarithmic concentration of Na_3VO_4. The half-maximal inhibitory concentration (IC_{50}) value obtained was approximately 8.36 μM, which is comparable to previously reported results [49]. This result confirmed the potential of the proposed sensing system for screening inhibitors.

4 Conclusions

In conclusion, $FeWO_4$ nanomaterials with intrinsic peroxidase activity were prepared through a one-step hydrothermal synthesis, and FWO-0.7, with the best catalytic activity, was selected and successfully applied in the PPi and

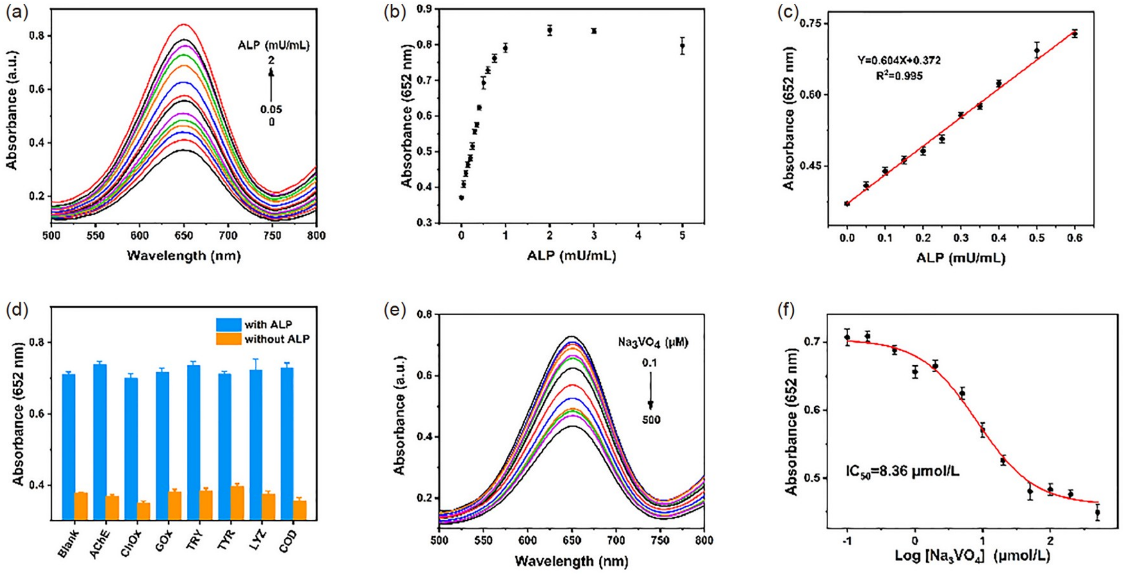

Figure 6 (a) UV-vis spectra and (b) absorbance of the FWO-0.7 colorimetric system with different activities of ALP at 652 nm. (c) The fitting linear curve of absorbance at 652 nm and ALP levels. (d) The effect of other substrates on the UV absorption spectrum at 652 nm with and without ALP, and other substrate concentrations of 100 mU/mL of GOx, TRY, TYR, LYZ, and COD; 10 mU/mL of AChE and Chox. (e) UV-vis spectra of the FWO-0.7 colorimetric system with different concentrations of Na_3VO_4. (f) The IC_{50} fitting curve of Na_3VO_4 concentration and inhibition efficiency in the presence of ALP (color online).

ALP assays. In detail, $FeWO_4$ nanomaterials with varied catalytic activities could be obtained by adjusting their size and oxygen vacancy of $FeWO_4$, and the order of the catalytic activities was as FWO-0.7 ≈ FWO-0.9 > FWO-0.5 > FWO-0.3 > FWO-0.1> FWO-0. The kinetic data indicated that the catalytic activity of the resulting mimetic enzyme exceeded those of most reported mimetic enzymes. Furthermore, the reaction mechanism experiments indicated that H_2O_2 first bound to the Fe atoms on the $FeWO_4$ nanomaterials, generating various ROS, which subsequently oxidized TMB to blue oxTMB. Therefore, a highly sensitive mimetic enzyme-based sensing platform for ALP and PPi was successfully established with a low detection limit, and it performed better than most of the current mimetic-enzyme-based sensors in the determination of ALP and PPi levels. Based on this, the assay system was further successfully used in real samples and inhibitor screening experiments. Finally, we expect that this study will provide new insights and potential applications for the design of mimetic enzyme materials in biological analysis.

Acknowledgements This work was supported by the National Natural Science Foundation of China (21974132, 22034006, 21721003) and the Open Project of State Key Laboratory of Supramolecular Structure and Materials (sklssm2023021).

Conflict of interest The authors declare no conflict of interest.

Supporting information The supporting information is available online at chem.scichina.com and link.springer.com/journal/11426. The supporting materials are published as submitted, without typesetting or editing. The responsibility for scientific accuracy and content remains entirely with the authors.

1 Zhao D, Ma X, Li N, Wang F, Chen C, Sun J. *Chin J Anal Chem*, 2021, 49: 1804–1815
2 Sun J, Zhao J, Bao X, Wang Q, Yang X. *Anal Chem*, 2018, 90: 6339–6345
3 Shi D, Sun Y, Lin L, Shi C, Wang G, Zhang X. *Analyst*, 2016, 141: 5549–5554
4 Lu D, Qin M, Zhao Y, Li H, Luo L, Ding C, Cheng P, Su M, Li H, Song Y, Li J. *Small*, 2023, 19: 2206461
5 Macrae MX, Blake S, Jiang X, Capone R, Estes DJ, Mayer M, Yang J. *ACS Nano*, 2009, 3: 3567–3580
6 Zhao D, Li J, Peng C, Zhu S, Sun J, Yang X. *Anal Chem*, 2019, 91: 2978–2984
7 Pandey S, Sharma AK, Sharma KH, Nerthigan Y, Khan MS, Hang DR, Wu HF. *Sens Actuat B-Chem*, 2018, 254: 514–518
8 Ye K, Wang L, Song H, Li X, Niu X. *J Mater Chem B*, 2019, 7: 4794–4800
9 Xi CY, Zhang M, Jiang L, Chen HY, Lv J, He Y, Hafez ME, Qian RC, Li DW. *Sens Actuators B*, 2022, 369
10 Liu H, Li M, Xia Y, Ren X. *ACS Appl Mater Interfaces*, 2017, 9: 120–126
11 Ruan C, Wang W, Gu B. *Anal Chem*, 2006, 78: 3379–3384
12 Lin Z, Luo S, Xu D, Liu S, Wu N, Yao W, Zhang X, Zheng L, Lin X. *Analyst*, 2020, 145: 424–433
13 Pathak RK, Tabbasum K, Rai A, Panda D, Rao CP. *Anal Chem*, 2012, 84: 5117–5123
14 Bhowmik S, Ghosh BN, Marjomäki V, Rissanen K. *J Am Chem Soc*, 2014, 136: 5543–5546
15 Wang W, Wu M, Liu H, Liu Q, Gao Y, Zhao B. *Tetrahedron Lett*, 2019, 60: 1631–1635
16 Anbu S, Paul A, Stasiuk GJ, Pombeiro AJL. *Coord Chem Rev*, 2021, 431: 213744
17 Lee DH, Kim SY, Hong JI. *Angew Chem*, 2004, 116: 4881–4884
18 Al-mashriqi HS, Zheng H, Qi S, Zhai H. *J Mol Structure*, 2021, 1242: 130755
19 Lee S, Yuen KKY, Jolliffe KA, Yoon J. *Chem Soc Rev*, 2015, 44: 1749–1762
20 Yıldırım D, Gökçal B, Büber E, Kip Ç, Demir MC, Tuncel A. *Chem Eng J*, 2021, 403: 126357
21 Markel U, Sauer DF, Wittwer M, Schiffels J, Cui H, Davari MD, Kröckert KW, Herres-Pawlis S, Okuda J, Schwaneberg U. *ACS Catal*, 2021, 11: 5079–5087
22 Wang L, Ye K, Pan J, Song H, Li X, Niu X. *Anal Methods*, 2019, 11: 5472–5477
23 Liu SG, Han L, Li N, Xiao N, Ju YJ, Li NB, Luo HQ. *J Mater Chem B*, 2018, 6: 2843–2850
24 Wang C, Gao J, Cao Y, Tan H. *Anal Chim Acta*, 2018, 1004: 74–81
25 Zhao Y, Li F, Li W, Li Y, Liu C, Zhao Z, Shan Y, Ji Y, Sun L. *Angew Chem Int Ed*, 2021, 60: 20331–20341
26 Bhosale R, Jain S, Vinod CP, Kumar S, Ogale S. *ACS Appl Mater Interfaces*, 2019, 11: 6174–6183
27 Xiao Z, Peng C, Jiang X, Peng Y, Huang X, Guan G, Zhang W, Liu X, Qin Z, Hu J. *Nanoscale*, 2016, 8: 12917–12928
28 Wang Z, Qian G, Yu T, Chen J, Shen F, Luo L, Zou Y, Yin S. *Chem Eng J*, 2022, 434: 134669
29 Lian J, Liu P, Liu Q. *J Hazard Mater*, 2022, 433: 128766
30 Boudghene Stambouli H, Guenfoud F, Benomara A, Mokhtari M, Sönmez-Çelebi M. *Reac Kinet Mech Cat*, 2021, 133: 563–578
31 Irfan M, Zahid M, Tahir N, Yaseen M, Qazi U. Y, Javaid R, Shahid I. *Int J Environ Sci Technol*, 2022
32 Yang Y, Logesh K, Mehrez S, Huynen I, Elbadawy I, Mohanavel V, Alamri S. *Ceram Int*, 2023, 49: 2130–2139
33 He GL, Chen MJ, Liu YQ, Li X, Liu YJ, Xu YH. *Appl Surf Sci*, 2015, 351: 474–479
34 Gao Q, Liu Z. *Prog Nat Sci-Mater Int*, 2017, 27: 556–560
35 Ojha DP, Karki HP, Song J, Kim HJ. *Chem Phys Lett*, 2018, 712: 83–88
36 Liao J, Chen L, Sun M, Lei B, Zeng X, Sun Y, Dong F. *Chin J Catal*, 2018, 39: 779–789
37 Schuler R, Bianchini F, Norby T, Fjellvåg H. *ACS Appl Mater Interfaces*, 2021, 13: 7416–7422
38 Li J, Xiao C, Wang K, Li Y, Zhang G. *Environ Sci Technol*, 2019, 53: 11023–11030
39 Wang H, Wang C, Cui X, Qin L, Ding R, Wang L, Liu Z, Zheng Z, Lv B. *Appl Catal B-Environ*, 2018, 221: 169–178
40 Ou G, Xu Y, Wen B, Lin R, Ge B, Tang Y, Liang Y, Yang C, Huang K, Zu D, Yu R, Chen W, Li J, Wu H, Liu LM, Li Y. *Nat Commun*, 2018, 9: 1302
41 Zhou YX, Yao HB, Zhang Q, Gong JY, Liu SJ, Yu SH. *Inorg Chem*, 2009, 48: 1082–1090
42 Su L, Feng J, Zhou X, Ren C, Li H, Chen X. *Anal Chem*, 2012, 84: 5753–5758
43 Liu S, Shu R, Ma J, Dou L, Zhang W, Wang S, Ji Y, Li Y, Xu J, Zhang D, Zhu M, Song Y, Wang J. *Chem Eng J*, 2022, 446: 137382
44 Zhang C, Ni P, Wang B, Liu W, Jiang Y, Chen C, Sun J, Lu Y. *Chin Chem Lett*, 2022, 33: 757–761
45 Wang Z, Dong K, Liu Z, Zhang Y, Chen Z, Sun H, Ren J, Qu X. *Biomaterials*, 2017, 113: 145–157
46 Yang J, Yao H, Guo Y, Yang B, Shi J. *Angew Chem Int Ed*, 2022, 61: e202200480
47 Zhou X, Wang M, Wang M, Su X. *ACS Appl Nano Mater*, 2021, 4: 7888–7896
48 Shi W, Li T, Chu N, Liu X, He M, Bui B, Chen M, Chen W. *Mater Sci Eng-C*, 2021, 129: 112404
49 Wu D, Zhao Q, Sun J, Yang X. *Chin Chem Lett*, 2023, 34: 107672